The distinct morphologic signature of underplating and seamounts in accretionary prisms, insights from thermomechanical modeling applied to Coastal Iranian Makran

Sepideh Pajang, Mohammad Mahdi Khatib, Mahmoudreza Heyhat, Nadaya Cubas, Eloise Bessiere, Jean Letouzey, Mohammad Mokhtari, Laetitia Le Pourhiet

The distinct morphologic signature of underplating and seamounts in accretionary prisms, insights from thermomechanical modeling applied to Coastal Iranian Makran

Sepideh Pajang[1,2], Mohammad Mahdi Khatib[2], Mahmoudreza Heyhat[2], Nadaya Cubas[1], Eloise Bessiere[1], Jean Letouzey[1], Mohammad Mokhtari[3], and Laetitia Le Pourhiet[1]

[1]Institut des Sciences de la Terre Paris, ISTeP UMR 7193, Sorbonne Universite, CNRS-INSU, 75005 Paris, France
[2]Geoscience department, University of Birjand, Birjand, Iran
[3]International Institute of Earthquake Engineering and Seismology (IIEES), Tehran, Iran

November 2022

Abstract

The active structures of the Iranian Makran, especially the presence of normal faults, vary laterally in the upper plate of the subduction zone, and their relationship with the deep duplexes and seamounts at depth remains unknown due to poor coverage of data onshore. In this paper, we investigate the relationship between deep structures and the topographic slope using thermo-mechanical simulations. The initial and boundary conditions of the models, including basal heat flux and convergence rate, are calibrated using the depth of the seafloor, bottom seafloor reflectors and the few available well temperature. We specifically test the influence of seamount subduction and thermally controlled changes in rock strength and décollement on the relationship between topography and deep tectonic structures. The inclusion of the brittle-ductile transition and dehydration reactions like the smectite-illite transition produce the three slope segments observed in the Makran accretionary prism. The three segments correspond to a regular accretionary prism, a flat segment that marks the smectite-illite transition, and a rise in topography located above the zone where the tegument reaches its temperature-controlled brittle-ductile transition causing underplating. Nevertheless, the models show that neither the decrease in friction associated with dehydration nor the onset of underplating is sufficient for the observed normal faults to arise in a self-consistent manner from the simulations. Crustal-scale normal faults only emerge in simulations that include subduction of a large seamount. These simulations also produce a large-thrust-slice that is the scar of former subducting seamount and serves as a buttress for the formation of a new imbricated zone. Using offshore seismic reflection data, the published onshore tomographic profiles, and our thermo-mechanical simulations, we propose two onshore-offshore cross-sections of the Iranian Makran accretionary prism.

Published in Tectonophysics

doi:10.1016/j.tecto.2022.229617

highlights

- First heat flow estimate from the Bottom Simulating Reflector (BSR) in Iranian Makran
- Models confirm that the regional Quaternary uplift of coastal Makran is due to underplating

- Underplating marks the onset of brittle-ductile transition at the base of the sediments
- Large-thrust-slice zone marks the geological signature of seamount subduction
- Deep-rooted listric normal faults are indicators of basal erosion by seamount subduction

keyword

Coastal Iranian Makran Heat flow Brittle-ductile transition Seamount subduction

1 Introduction

The Makran accretionary prism (MAP), located in SE Iran and SW Pakistan, is the largest accretionary wedge in the world, e.g. (Burg, 2018). Makran is the result of the ongoing oceanic part of Arabian plate subducting beneath Eurasia since the Early Cretaceous. The subduction rate increases from 35.5 - 36.5 mm yr^{-1} to 39 mm yr^{-1} from west to east (DeMets et al., 2010); (Figure 1). The MAP is located between two major collisional zones, Zagros to the West and Himalaya to the East (Figure 1). Active transitions between these collisional domains are accommodated by two major strike-slip fault systems, the Ornach Nal fault to the East, and the Minab-Zendan fault to the West (Figure 1). The MAP is characterized by high sedimentation rates related to the Himalayan orogeny (Kopp et al., 2000; Kukowski et al., 2001; Schlüter et al., 2002; Grando and McClay, 2007) or other local sources (Mohammadi et al., 2016). It is about $\sim$ 1000 km long and $\sim$ 400 km wide region (Farhoudi and Karig, 1977), and two-thirds of it are exposed onshore. The subducting plate has a northward dip of 2° until 27°N, then it bends down with a dip angle of 30° (Kopp et al., 2000; Kukowski et al., 2001).

The Makran accretionary prism is classically divided into two areas, the offshore area characterized by a classic imbricated zone (Grando and McClay, 2007; Burg, 2018; Pajang et al., 2021), and the onshore area, which can be subdivided into four tectonic units based on the age of deformation (Burg et al., 2008; Dolati, 2010). From North to South, these units are (1) North Makran - Cretaceous, (2) Inner Makran Eocene-Oligocene, (3) Outer Makran - Early-Middle Miocene, and (4) Coastal Makran - Late Miocene - Pleistocene (Figure 1). A large submarine olistostrome dated to Tortonian (between 11.8 and 7.2 Ma) that crops out along the Inner, Outer, and some part of Coastal Iranian Makran (Burg et al., 2008; Ruh et al., 2018) indicates that the wedge was still completely submarine until $\sim$ 9-12 Ma. The olistostrome is a non-metamorphic formation. This shaly matrix-supported formation contains randomly mixed blocks of various compositions (limestones, sandstones, shales, cherts, schists, pillow lava, gabbros, and serpentinites), sizes and shapes from millimetric to kilometric scale (Burg et al., 2008). The emersion of the prism was accompanied by growth structures of the Late Miocene to Early Pliocene age (Dolati, 2010) until the compressional deformation ceased in the coastal area in the Late Pliocene to migrate to its current imbricated complex offshore (Platt et al., 1988).

Our study focuses on coastal and offshore Makran located south of the Chah Khan thrust fault (CKT) (Figure 2a); (Burg et al., 2008). These areas constitute the most recent and still deforming area of Makran (Haghipour et al., 2012). They comprise Late Miocene-Quaternary shallow-marine marl-dominated and calcareous sandstone-dominated sediments that have been folded along *en échelon* synclines (Platt and Leggett, 1986). The coarsening-up from mudstone-dominated to sandstone-dominated sequences with abundant bioturbation by marine gastropods in the late Pliocene represents the transition from the shallow marine shelf into foreshore deltaic and fluviatile conditions. It appears before the deposition of a coarse fan of Pleistocene age that lies in unconformity over large areas of southern Makran (Mohammadi et al., 2016; Burg, 2018). Nonetheless, the Quaternary surface uplift of coastal Makran is indicated by elevated marine terraces along the Makran coast (Falcon, 1975; Vita-Finzi, 1975;

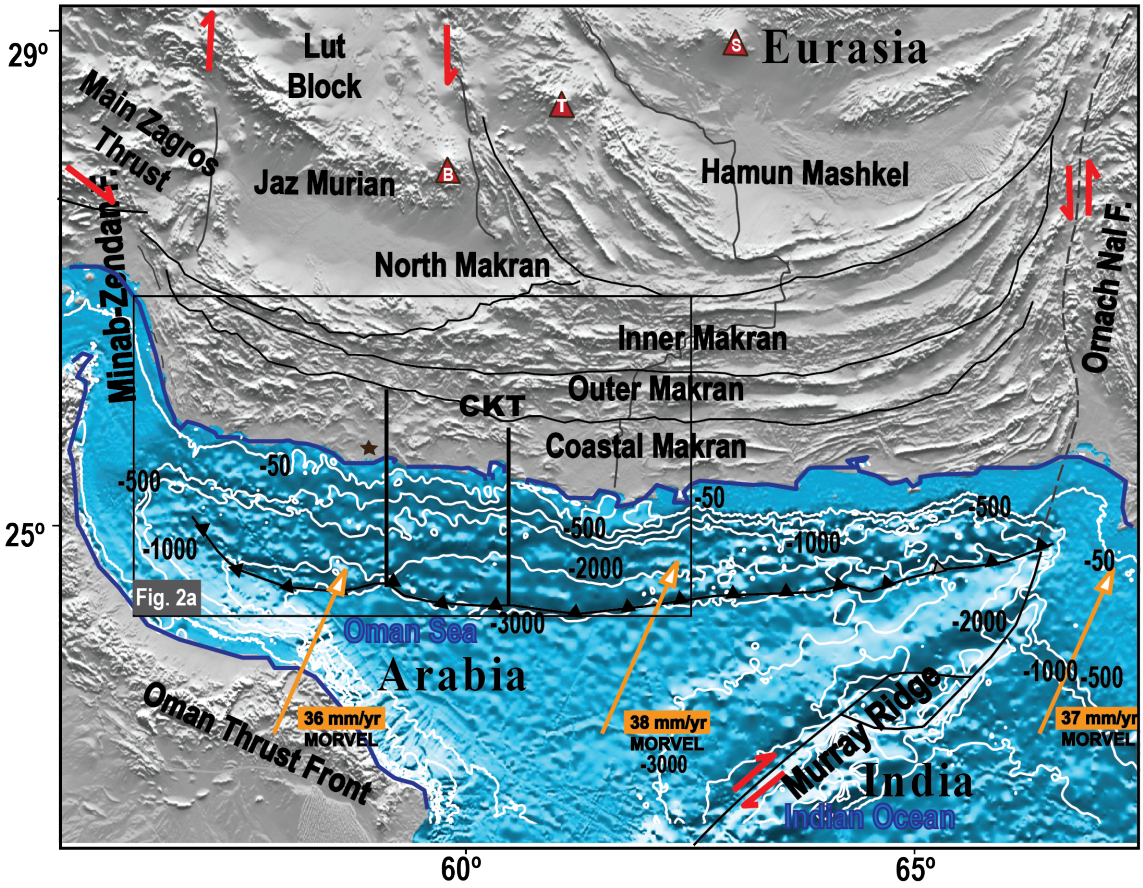

Figure 1: Geodynamic setting of Makran. Straight black lines indicate the location of the cross-sections of this contribution. White iso-contours indicate the bathymetry in meters. Orange arrows are MORVEL velocities from (DeMets et al., 2010), CKT: Chah Khan thrust. The onshore well in Iran is indicated by a star. Brown triangles indicate the positions of the Pleistocene volcanoes related to the subduction of the Arabian plate underneath the Eurasian plate (the Bazman, Taftan, and Soltan).

Page et al., 1979). The mean Pleistocene uplift of the Makran coast was estimated at 0.2 mm.yr^{-1} from marine terraces (Page et al., 1979) and $\sim$ 0.3 mm.yr^{-1} of fluvial incision (Haghipour et al., 2015) in the western to 0.5 - 2 mm.yr^{-1} in the eastern Makran. The Holocene coastal uplift was faster, 2 mm.yr^{-1} (Page et al., 1979) or 3 mm.yr^{-1} (Haghipour et al., 2015). The recent Pliocene emersion of coastal Makran has been attributed to the onset of underplating (Platt and Leggett, 1986; Burg, 2018), and internal pure shear deformation driven by weak olistolithic units with salt-like mechanical behavior (Ruh et al., 2018). Recent simulations of accretionary prism including the thermo-mechanical coupling and temperature dependent rheologies (Pajang et al., 2022) suggest that the onset of ductile deformation associated with splay faults could also explain this phase of rapid uplift, which started in the Pliocene and is still ongoing. Today, the offshore and onshore areas are separated by a narrow (few kilometers wide) yet not completely continuous coastal belt along which normal faults and mud volcanoes are prominent, e.g. (Kukowski et al., 2001; Schlüter et al., 2002; Grando and McClay, 2007; Babadi et al., 2019; Normand et al., 2019).

Together with offshore seismic data, we have used the geological maps of the coastal area, literature, and 30 m digital elevation model (DEM) data of coastal Iran to build an integrated geological map of Makran including both on and offshore areas (Figure 2a) on which we base our new cross-sections. The profiles are oriented perpendicular to the average strike of the bedding (E-W) in continuity with offshore cross-sections. They are drawn from the two NS seismic profiles (PC 2000, commercial seismic reflection data) of the Persian carpet that cover the complete prism from the deformation front to the coast. Their detailed interpretation is discussed in Pajang et al. (2021). The Eastern section cuts across an area where normal faults are documented onshore, while the central section cuts across an area with no active normal faults. The central profile does not display large normal faults but deep duplexes along the shoreline (Figure 2c). Compared with eastern and western parts, it presents a larger diapiric zone, and the imbricated zone at the toe of the wedge is affected by a seamount entering into subduction (Pajang et al., 2021). We note that this seamount is probably not the only one of this kind in the area, as the recent tomographic model (Haberland et al., 2020) also suggests the presence of seamounts underneath onshore areas. Along the eastern profile (Figure 2b), three different structural domains have been defined (Grando and McClay, 2007; Pajang et al., 2021): (1) a north-dipping imbricated thrust zone at the front, followed by (2) a diapiric zone of shallow origin, and (3) active listric normal faults, located along the shoreline, that seem to root down to the décollement. These three domains have been associated with three distinct topographic gradients described by Kukowski et al. (2001) as slope, middle slope, and lower slope in Figure 2a.

The origin of these normal faults is debated. Some studies posit these normal faults are shallow gravitationally driven structures (Grando and McClay, 2007) related to underplating, which increases surface slope and leads to a jump at the maximal critical value generating normal faults (Ruh, 2017; Ellouz-Zimmermann et al., 2007b; Haghipour et al., 2012). Yet, based on seismic profiles, Pajang et al. (2021) have interpreted these faults as large-scale listric normal faults rooting on the main décollement. In the latter case, their activation or reactivation requires a drastic change in basal friction according to limit analysis (Cubas et al., 2013; Pajang et al., 2021).

As a large part of the coastal Makran region is covered with Quaternary sediments and due to the lack of subsurface data from the coastal areas, the link between off and onshore structures, especially at depth, remains unknown. The poor quality of seismic data at depth and its small coverage at the border of the coastal area make its structural determination difficult. Therefore, the relationships between the deep structure, the normal faults, the décollement, and the pre-existing thrust faults remain unclear. To better understand the Quaternary evolution along the Iranian Makran, it is essential to get a better knowledge of the geometry and dynamic of the structures responsible for the uplift of the coastal area. In this respect, we perform thermo-mechanical simulations which include thermally controlled changes in basal and internal strengths (Pajang et al., 2022) calibrated to Makran using new heat flow estimates from the Bottom Simulating Reflector (BSR). The simulation results are then used to propose two on-

offshore crustal cross-sections, which integrate constraints from offshore seismic profiles and the recent tomographic model of coastal Makran (Figure 2b, c); (Haberland et al., 2020).

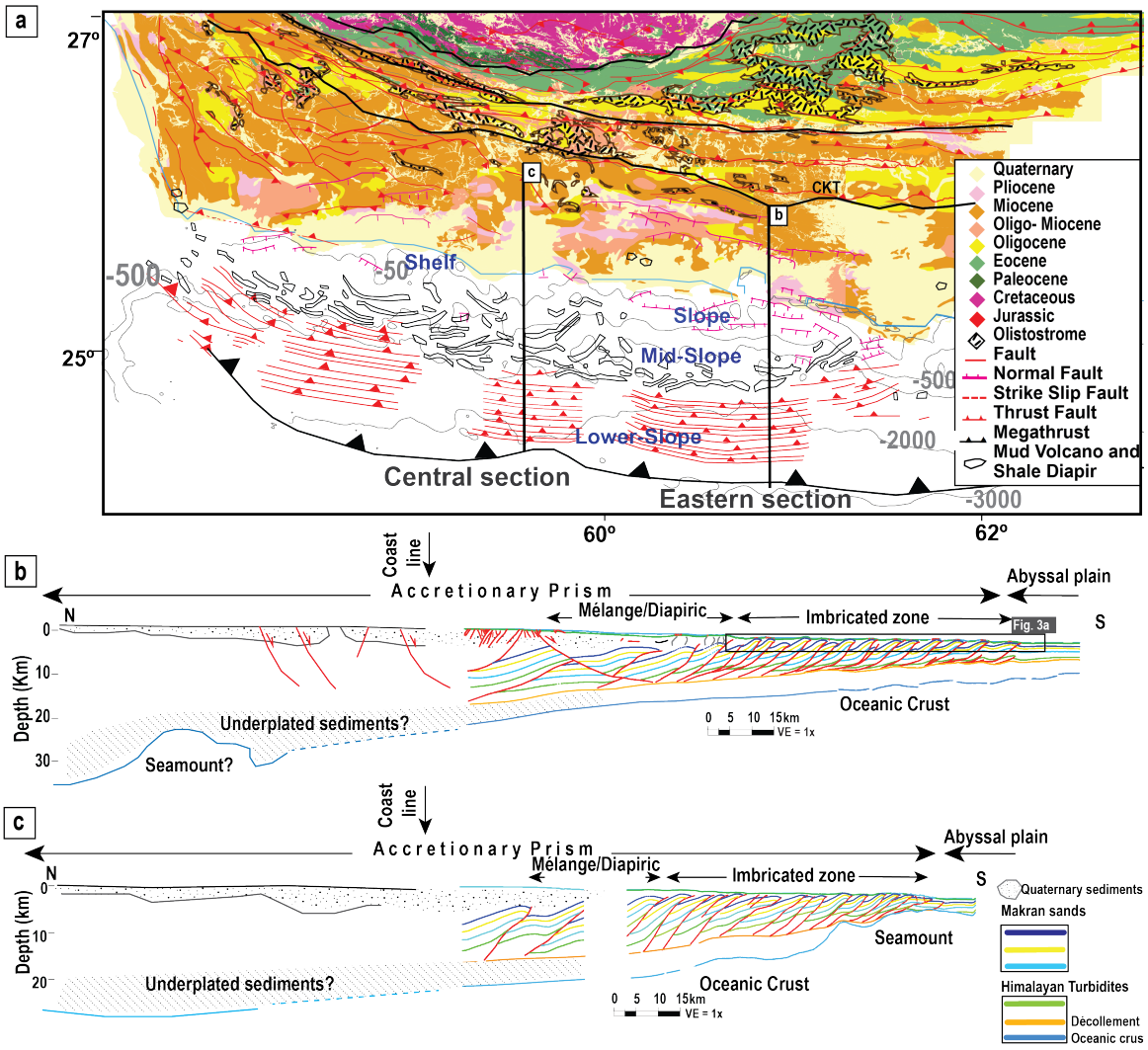

Figure 2: **a.** Structural map (offshore is taken from Pajang et al. (2021)) overlaid with the age distribution of outcrops and the location of the Olistostrome from Burg et al. (2008). **b.** Eastern and **c.** Central cross-sections migrated in depth. The offshore part is taken from Pajang et al. (2021) and the onshore from Haberland et al. (2020).

2 Modeling incentive and calibration of the models

2.1 Need for a thermo-mechanically coupled model of Makran

Pajang et al. (2022) have shown that increasing temperature with burial affects the modes of deformation and the growth of topography. They account for the dependence of effective basal friction on temperature due to metamorphic reaction or brittle-ductile transition. Simulations of an accretionary prism with a single décollement layer display three stages of growth associated with distinct signatures in terms of the topographic slope. The slope of an initial purely frictional stage is directly related to the basal friction of the décollement. The second stage is marked by an increase in the topographic

slope, which corresponds to the onset of ductile deformation in between brittle structures while the décollement is still brittle. The last stage of deformation corresponds to the beginning of ductile deformation along the décollement in the most thickened parts of the accretion prism. Once the accretionary prism has been through sufficient accretion to reach this last stage, the wedge reaches a steady state shape and a flat plateau forms at its back. This plateau widens with time and is bounded by a large slope corresponding to splay faults rooting at the brittle-ductile transition which act as a backstop to a brittle wedge following the critical taper theory. The amount of deformation to reach the brittle-ductile transition stage decreased with increasing basal heat flow, heat production within the wedge, the thickness of the incoming sediment pile, and erosion-sedimentation rate. Since Makran is one of the thickest accretionary prisms in the world, the contribution of heat to the rheology of the prism cannot be ignored. Moreover, although including temperature evolution in a model of accretionary prism adds to the number of parameters in the simulation, most of them can be calibrated with the seismic data available in Makran, which displays a clear BSR. This permits to complexify the physics without increasing the number of uncertain parameters.

Platt and Leggett (1986) and Burg et al. (2012) proposed that the emersion of Makran was caused by the underthrusting of the sediments located underneath the shales which act as a décollement in the offshore section. Previous analogue and numerical experiments of wedge systems have shown that the presence of an intermediate décollement is essential for underthrusting to occur at the rear of the wedge (Bonnet et al., 2007; Stockmal et al., 2007; Kukowski et al., 2002; Ruh et al., 2012; Ruh, 2017, 2020). Here, we follow the same approach using two décollements, yet we include thermal coupling effects.

To do so, we use pTatin2d (May et al., 2014, 2015), the governing equations and rheological laws are detailed in the Appendix. All experiments with their parameters are listed in Tables 1 and 2.

Model	k	DR	Seamount
1	1×10^{-6}	off	-
2	1×10^{-5}	off	-
3	1×10^{-6}	on	-
4	1×10^{-6}	on	type 1
5	1×10^{-6}	on	type 2
6	1×10^{-6}	on	type 3

Table 1: Variable parameters between experiments. k: coefficient of diffusion for a surface process model, DR: dehydration reaction.

2.2 Set up and Boundary Conditions

The depth-migrated profiles are available in Pajang et al. (2021). The length of the eastern profile is 140 km from the coast to the deformation front, with a maximum water depth of ~ 3400 m. The profile is characterized by a large seaward normal fault that seems to root down to the décollement, a shale diapiric zone, and the imbricated thrust zone. The 78 km long imbricated zone is composed of seventeen thrust sheets that branch from a shallow décollement at ~ 3.5 km depth. The slab dip is $\sim 2°$. The central profile clearly displays a seamount entering the accretionary prism at the front and shows no evidence of a large normal fault at the back.

Using these geometric constrains, the model domain is 500 km long and its initial thickness is 7.5 km. It consists of 3 layers, two 500 m (thick) $\times$ 500 km and 500 m $\times$ 350 km décollements modeled by shale rheology, while the rest and between are modeled by sandstone-quartz rheology. The shallow décollement corresponds to the one identified on the seismic lines. It is described either as an Eocene overpressured shale sourced from the Himalayan Turbidites (Grando and McClay, 2007) or

the Mid-Miocene Parkini mudstones (Ellouz-Zimmermann et al., 2007a; Schlüter et al., 2002). The deep décollement of the model is more hypothetical and corresponds to the top of the oceanic crust. The domain is discretized with a mesh of 512×24 Q2 elements (Figure 3). The resolution is therefore 1 km in the x-direction. In the y-direction, the resolution varies with the thickness of the model to accommodate the deformation of the free surface. Moreover, as two mesh elements are aligned with the interface of the first and the second décollement layers to describe more accurately their friction at small strain (Figure 3), only the elements located above the shallow décollement may accommodate the topography. The right and bottom boundaries of the models have a constant velocity $V_x = 4$cm/yr. The current version of pTatin2d is not designed to impose velocity boundary conditions on an interface which normal is not the x or the y axis. In order to account for the 2° basal slope in the model, we therefore rotate the gravity field by 2°. This means that the x-axis of the model is not horizontal nor is the sea level that is defined as y = 3400 m above the undisturbed sediments on the right side of the model. Above this approximated sea level, the domain is modeled with a free surface, and below additional normal stress is applied on the deformed surface to mimic weight of the water but the shear stress remains zero like above the sea level. The décollement possesses a finite thickness that is considered part of the domain. As such, the basal shales are allowed to be dragged from the finite thickness the décollement into the rest of the model domain unlike in the two methods employed to benchmark the numerical code with sandbox experiments (Buiter et al., 2016).

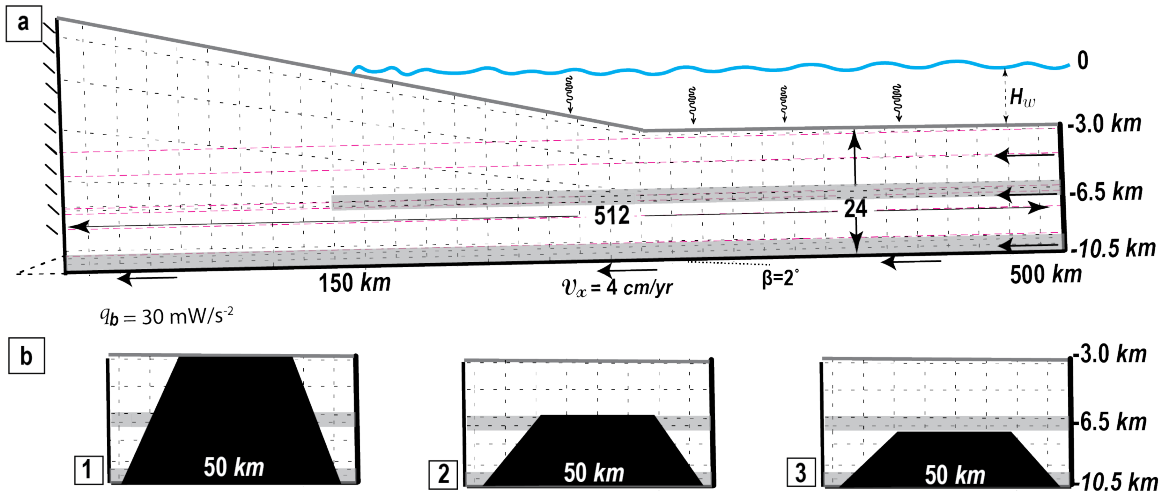

Figure 3: **a.** Model set-up. Boundary conditions are a non-deformable backstop on the left side, a constant velocity in the x-direction of 4 cm.year^{-1}, free surface or water pressure considered below sea level and basal heat flow calibrated from BSR. **b.** Three different initial seamount geometries.

The thermal boundary conditions assign the temperature $T_0 = 0°C$ at the surface and null horizontal heat flow on the y-normal walls of the domain. As we assume no radiogenic heat production, the initial temperature in the domain is fixed using a constant thermal gradient reaching an initial bottom temperature that depends on basal heat flow (see Section 2.3). The simulations include shear heating (see Appendix for more details) but as fluids circulations are not simulated explicitly advection of heat is only carried by rocks.

Tomographic models (Haberland et al., 2020) running close to our cross-sections indicate packages with a higher velocity at depth underneath the land sections. They have so far been interpreted as localized underplating based on available numerical and analogue models. However, these bodies show P-wave velocities that are large enough to represent seamounts. Given that our central section is affected by a seamount, and that, so far, no model of seamount subduction including temperature

transition effects has been published; we decided to test the impact of seamount subduction on the deformation of an accretionary prism.

In some of our simulations, we also intend to account for fluid overpressure due to roughly dehydration of shale materials between 110 to 145 $°C$, which potentially corresponds to the smectite-illite transition as followed by Pajang et al. (2022). We posit that for temperature lower than $110°C$, the internal friction angle of the décollement containing smectite is $\phi_b = 5°$. We then arbitrarily drop the friction angle from 5 to 0.1 degrees between 110 to 145 $°C$ to reflect a fluid overpressure due to ongoing dehydration. Doing so, we assume that fluid overpressure rebuilds after each event of brittle failure as long as the décollement is dehydrating. Finally, we assume that once the dehydration is complete, that is, for temperature above 145 $°C$, the shaly décollement is illite rich. From that point, the internal friction angle of the shally décollement is set to 10° assuming that illite is more frictional than smectite and that there is no more fluid source to maintain fluid overpressure.

Parameter	Name	Unit	Sandstone[a]	Shale[b]	Sediment[a]	Diabase
A	Pre-exponential factor	$MPa^{-n}.s^{-1}$	6.8×10^{-6}	1.3×10^{-67}	6.8×10^{-6}	6.3×10^{-2}
n	Stress exponent	-	3	31	3	3.05
Q	Activation energy	kJ	156	98	156	276
C_0	Initial cohesion	MPa	2	0.1	2	2
C_∞	Final cohesion	MPa	1	0.1	1	1
ϕ_0	Initial friction	^{o}	20	5-0.1-10$^{\bowtie}$	20	30
ϕ_∞	Final friction	^{o}	10	5-0.1-10$^{\bowtie}$	10	30
κ	Heat diffusivity	$m^2.s^{-1}$	10^{-6}	10^{-6}	5×10^{-7}	10^{-6}
ρ	Density	$kg.m^{-3}$	2400	2400	2000	2900

Table 2: Variable rheological parameters and coefficients for the different lithologies; creep parameters [a] from (Ranalli and Murphy, 1987) and [b] from (Shea and Kronenberg, 1992). $\bowtie$ The friction of shale depends on peak temperature rather than plastic strain.

2.3 Calibration from BSR

The basal heat flow of young plates can usually be estimated from the age of the oceanic basement deduced from magnetic anomalies using the half-space cooling model or a plate cooling model with a maximum plate thickness of 95 km (Turcotte and Schubert, 2002). However, there are some places like the North Arabian Sea, where due to the lack of magnetic anomaly, the oceanic lithosphere age remains uncertain (Ellouz-Zimmermann et al., 2007a) and alternative constraints need to be found. A few bottom hole temperature (BHT) i.e. the maximum recorded temperature during a logging run, exist for the Iranian wells in Makran. They indicate a temperature gradient of 20 $°C.km^{-1}$ (Skarpnes et al., 2003). Yet, it should be noted that the reliability of this datum is somewhat uncertain since the temperature data are rather old and there is no indication as to whether the maximum temperatures have been corrected for the thermal disturbances caused by drilling (from report onshore well in Iran). Nevertheless, these values are within the range of those calculated for five wells in the Pakistani part of Makran (20-23 $°C.km^{-1}$) by Khan et al. (1991).

Assuming that erosion and sedimentation processes are slow enough for temperatures to be at a steady state near the surface, heat flow can also be estimated from the Bottom Simulating Reflector (BSR), well data, and plate age. The BSR is a cross-cutting seismic reflector caused by small amounts of free gas trapped below the sealing gas hydrate layer (Skarpnes et al., 2003) which is thought to be the base of the hydrate stability zone and is approximately parallel to the seafloor (Ganguly et al., 2000). Phase diagrams of gas hydrate stability have been published from experimental data (MacLeod, 1982; Dholabhai et al., 1991; Dickens and Quinby-Hunt, 1994; Maekawa, 2001) and empirical and numerical

laws, e.g. (Englezos and Bishnoi, 1988; Miles, 1995; Sultan et al., 2004; Tishchenko et al., 2005). These diagrams can determine the approximate temperature at the base of the gas hydrate stability zone. This method has been applied to many accretionary prisms such as south America (Ecuador, Colombia, Chile, Perou); (Marcaillou et al., 2006; Villar-Muñoz et al., 2014, 2019; Quintero et al., 2019), Nankai (Grevemeyer and Villinger, 2001; Martin and Dahlen, 2005; Kinoshita et al., 2011; Ohde et al., 2018), Cascadia (Ganguly et al., 2000; Phrampus et al., 2017), and the Pakistani side of Makran (Hutchison et al., 1981; Kaul et al., 2000; Sain et al., 2000).

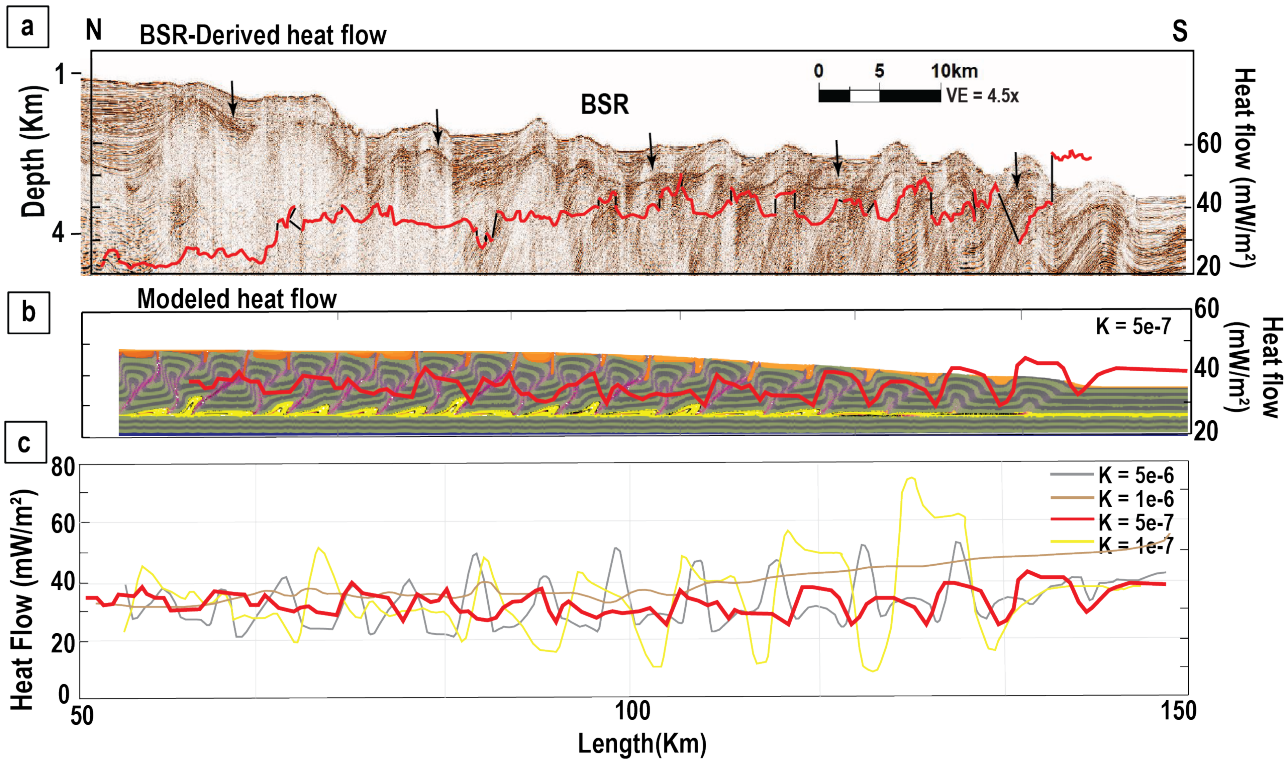

Figure 4: Comparison of heat flow derived BSR and models. **a.** Zoom-in of Eastern offshore migrated profile. The BSR is indicated by black arrows; the BSR-derived heat flow is shown in red. To better visualize sharp heat flow changes, the black lines join the offset red segments. **b.** A good fit between BSR-derived heat flow and model, reproducing the wiggles size and the pattern relative to thrusts and basins. **c.** Heat flow is extracted from different diffusivities of sediments.

In the Iranian part of the Oman Sea, the BSR is observed on nearly all the seismic lines with water depths greater than 1300 m. We picked the horizon of the BSR along the two depth migrated seismic profiles and interpreted in Pajang et al. (2021). In order to compute the temperature of the BSR, we used a salinity of 34.7 and 100 percent Methane together with the stability diagram of Tishchenko et al. (2005). Seafloor temperatures have been calculated according to a specific law considering the water temperature evolution through depth. Finally, the thermal conductivity of sediments is considered k= 1.19 $\mathrm{Wm^{-1}K^{-1}}$ based on Pakistani wells (Minshull and White, 1989). The heat flow q averaged between BSR and seafloor horizon, is then expressed as $q = -k\Gamma$, where $\Gamma = \frac{\mathrm{T_{BSR}} - \mathrm{T_{sea}}}{\mathrm{Z_{BSR}} - \mathrm{Z_{sea}}}$, is the geothermal gradient.

The BSR-derived heat flow is computed and shown in red along the eastern (Figure 4a) and central profiles (Figure Supp.10). The landward decrease in heat flow is explained by the landward deepening of the oceanic plate and accretion of cold sediments in the accretionary wedge (Hyndman and Wang, 1993). Values range between 27-43 $\mathrm{mWm^{-2}}$ with local anomalies that correlate with tectonic slices.

These local variations are similar to those observed by Minshull and White (1989) along the Pakistani side of Makran. In average, they agree with the well data (Khan et al., 1991). The correlation of anomalously high-temperature gradients with thrusts and their piggyback basins could either indicate fluid circulation (Ganguly et al., 2000) or result from the thermal blanketing effect due to the lower conduction in recent sediments.

As seen in Pajang et al. (2022), four parameters affect the thermal regime of the accretionary prism: basal heat flow, the thermal conductivity of recent sediments, shear heating, and the thickness of the incoming sediment pile. This last parameter is constrained by seismic data. Basal heat flow and thermal conductivity of sediments can be deduced from adjusting our models to the mean value (basal heat flow) and the deviation (thermal conductivity) of our BSR-derived heat flow. We varied the diffusivity of the recently deposited sediments to compare the model surface heat flow with the BSR-derived heat flow (Figure 4).

We find that a basal heat flow of 50 $mW.m^{-2}$ explains the long wavelength variation of the BSR, while a thermal diffusivity of $\kappa = 5 \times 10^{-7} m^2.s^{-1}$ in the sediment captures the amplitude of the heat flow anomalies associated with piggyback basins. From now on, all the presented simulations will be run with these parameters reaching an initial bottom temperature of 135°C.

2.4 Representation of results

For each simulation, frictional parameters are listed together with viscous parameters, density, and thermal diffusivity in Table 2. The finite brittle strain (accumulated plastic strain) in the rocks and the strain rate of the current state are shown for each model. The finite strain figure displays the lithologies of rocks and the accumulated plastic strain on markers with a linear colormap. Markers with values of plastic strain ε_p larger than 2 or 3 can be interpreted as part of a fault. Sandstone sequences have been colored with thin tracer layers that have no physical meaning but display the deformation. Brown to yellow colors indicate the deposition time of sediment markers deposited by the surface evolution model. The strain within deposited sediments can be deduced from the deformation of their bedding.

The current state figure displays whether the material is yielding plastically (medium gray), deforms viscously (dark gray), or does not deform at a rate larger than the $10^{-17}\mathrm{s}^{-1}$ threshold (light gray). It is overlaid by a representation of the $\dot{\varepsilon}_{xx}$ component of strain rate to outline active structures in red when they accommodate extension and in blue for shortening. A cut-off range of $-10^{-14}s^{-1}$ to $10^{-14}s^{-1}$ is used for the post-processing although the actual values span a larger range. We also represent the $110°C$ isotherm to locate the onset of the dehydration reaction, the $180°C$ isotherm which corresponds to the onset of viscous deformation and the $300°C$ for the brittle-ductile transition for quartz (Pajang et al., 2022). Finally, a color code at the top of the slice represents the local topographic slope.

3 Modeling results

3.1 Temporal evolution

Figure 5 displays the structural evolution of the reference simulation **M1** through time. The wedge grows by horizontal shortening and vertical thickening. Most shortening is accommodated by thrusting and brittle deformation along the frontal part. Some of the vertical thickening is accommodated by reactivation of thrusts within the wedge, the rest by underplating. Temperature changes concerning increasing depth affect the structure and surface slope.

Since there is no shallow décollement in the first 150 km of the model domain, the wedge is formed above the deep frictionally strong décollement. During the first 2 Myr, the initial wedge grows to reach its critical state generating a topographic slope ($\sim 7.3°$) corresponding to its basal friction $\phi_b = 10°$

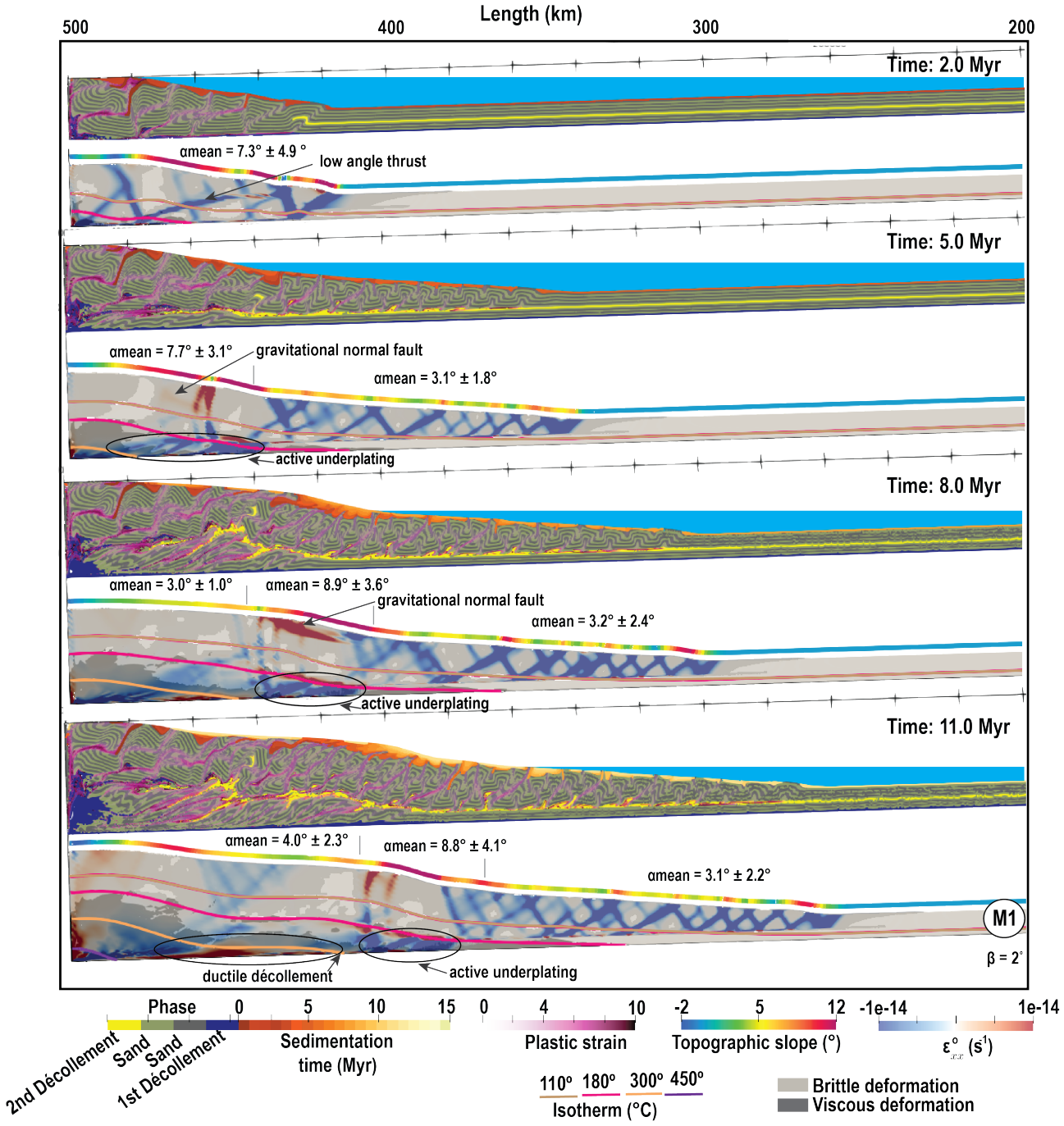

Figure 5: Temporal evolution of the reference model (**M1**) from beginning to 11 Myr of shortening, x and y-directions are along the model axis, 1 : 1 scale.

and internal friction $\bar{\phi}$=15^o (the average of $\phi_0 = 20^o$ and $\phi_\infty = 10^o$). The spacing between thrusts agrees with the initial thickness of 7.5 km. The time interval between the formation of two consecutive thrusts in this part of the model domain is 0.5 Myr. The horizontal component of the strain rate indicates a low angle thrust compatible with the large friction of the basal décollement.

As soon as the frictionally weaker shallow décollement starts to be involved (2 Myr, Figure 5), the strong basal one is abandoned, and the wedge propagates into a thinner imbricated thrust zone. As a result, the time interval between two new thrusts formation is reduced. Six faults may form in 1 Myr. After 5 Myr, the deformation has propagated along the weak shallow décollement. The horizontal component of strain rate indicates that the out-of-sequence activity of thrusts and steep back-thrusts tend to keep the frontal wedge at a critical state. Like in Pajang et al. (2022), the onset of activity of these structures corresponds with the onset of internal viscous deformation between the brittle structures and the frictionally strong basal décollement. These structures form as soon as the basal temperature reaches 180 °C. In these new simulations with two décollements, we find that the ductile activation of the basal décollement marks the onset of active underplating (4 Myr). The basal sequences of the model are underplated beneath the shallow décollement to establish a series of duplexes that lead to the thickening and uplift of the rear of the wedge after 8 Myr. The sharp transition in the topographic slope that separates the brittle frontal wedge from the thicker brittle-ductile wedge corresponds to the zone of active underplating. According to the critical taper theory, this segment of the wedge jumps from critical compression to critical extension, causing the formation of gravitational normal faults (in red, Figure 5). At the back of this large slope, as the temperature continues increasing with burial, it finally reaches 300 °C, i.e., the brittle-ductile transition for quartz at average strain-rate. These normal faults also affect the time formation of thrust faults at the front reaching eight thrusts per Myr. When the the deep décollement starts to display a fully ductile behavior (at $x = 445km$ after 8 Myr), and the topographic slope tends to flatten. From 11 Myr, the slope remains critical according to critical taper theory and constant at the front while the warm part of the wedge grows in length. The topography of the ductile part continues to flatten except at the corner of the model domain where a normal fault, which is most probably a boundary effect develops. Active underplating occurs between the crossing of the 180 to 300 °C isotherms with the bottom of the model domain.

3.2 Sensitivity to erosion / sedimentation rate

In figure 6, we first compare the results of our reference model (**M1**) with the model (**M2**) that is affected by larger erosion and sedimentation rates. This larger rate of sedimentation strongly modifies the geometry of the tectonic units at the frontal part of the wedge without modifying its slope. Instead of a small imbricated system, a smaller number of thrusts forms with a larger spacing between them and more developed piggyback basins. As erosion and sedimentation reduce the slope at every step, the wedge tries to recover its critical taper by the activation of back-thrusts along the frontal part and a larger amount of under-thrusting along the rear and deeper part. As sediments have a lower conductivity than rocks (thermal blanketing), higher heat flow localizes on active thrusts, and the temperature gradient of this model is larger (Pajang et al., 2022). As a result, underplating starts at earlier stages in model **M2**. However, underplating forms a large antiformal stack duplex at the rear of model **M2**, while it propagates towards the front in the model **M1**. This has important implication for the exhumation of material from the lower part of the wedge. The sequences above the décollement form a synform in front of the antiformal stack. This behavior is comparable to the effect of erosion described in many analogue models; see Konstantinovskaya and Malavieille (2011) for a review. In this model, the large rate of offshore sedimentation is not compatible with the geometry of the imbricated zone displayed in the seismic data offshore Makran.

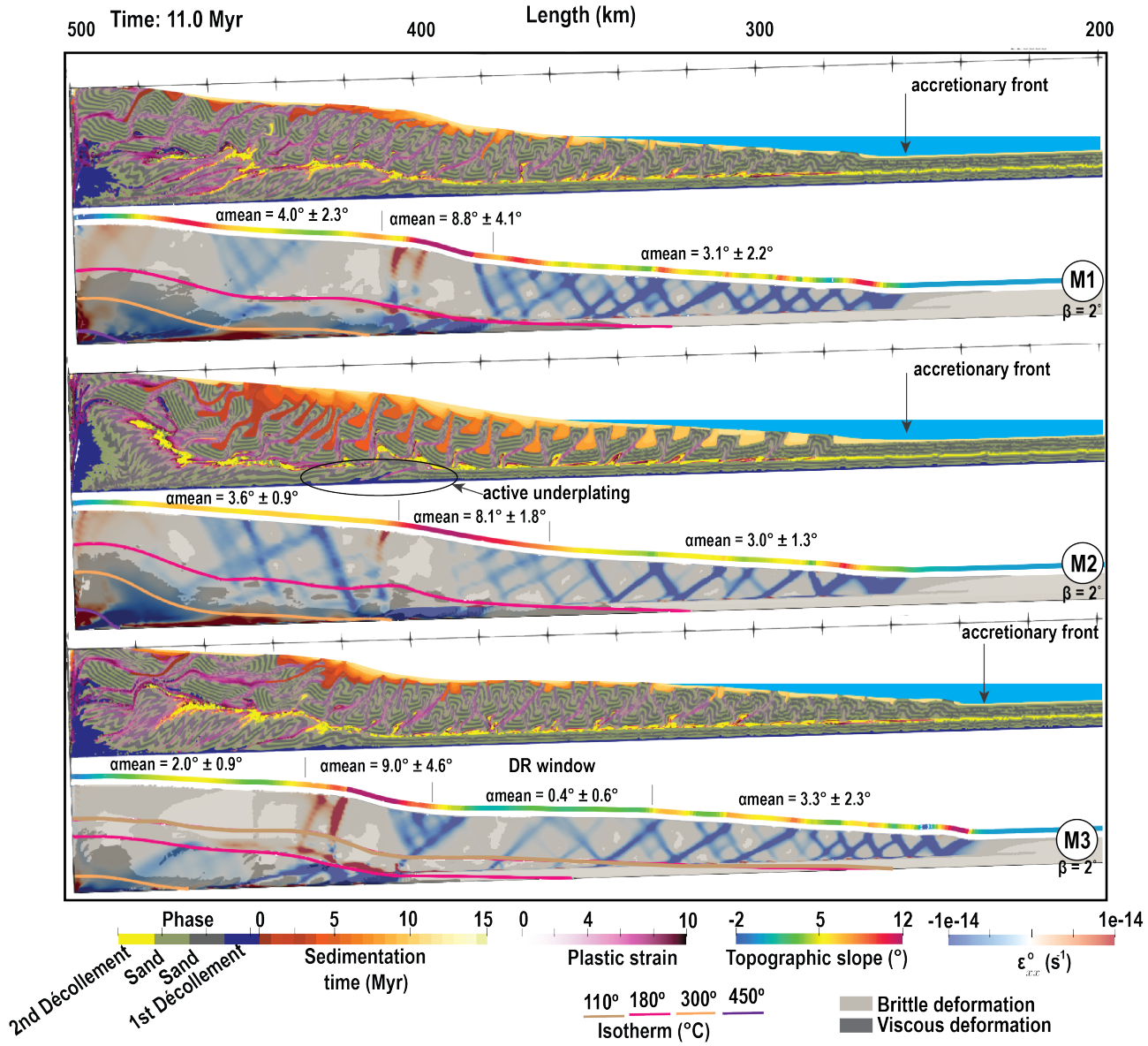

Figure 6: Model **M1**: with moderate erosion sedimentation diffusion coefficient compared to model **M2**: the same experiment with a larger erosion coefficient. Model **M3**: with the smectite-illite transition. All after 11 Myr evolution. The finite strain, the current state and strain rate are shown for an internal frictional softening drop from 20° to 10°. The yellowish-brown color illustrates syn-tectonic sedimentation in the form of piggyback basins, which representing a given age corresponding to the deposition time. Where the material is yielding plastically is in light grey or deforms viscously is in dark grey, with the onset of 180 and 300 °C isotherms. The local topographic slope with a color code shown at the top of the slice is affected by temperature and frictional properties, 1 : 1 scale.

3.3 Sensitivity to dehydration reactions

The frontal parts of the reference model and the dehydration reaction model (**M3**) display similar tapers and ramp spacing. However, when the temperature reaches $110°C$ at the depth of the shallow décollement and enter the dehydration reaction window, its friction drops as the model assumes the persistence of fluid overpressure. This leads to the formation of a flat topography (0.4 °, Figure 6 **M3**) which corresponds to the slope predicted by the critical taper theory for basal friction of $\phi_b = 0.1°$. As a result, the length of the frontal imbricated zone increases. In contrast to the imbricated zone forming above basal friction of $\phi_b = 5°$, the segment with low friction ($x = 330 - 390km$) displays almost no internal deformation. Once the shallow décollement exits the dehydration reaction window, between c.a. 145 to 180 ^{o}C temperature range, its friction increases back up to $\phi_b = 10°$, which results in a larger topographic slope. At about the same x-location, the deep décollement starts to follow a ductile behavior marking the onset of underplating. At the back of the model, deformation patterns are very similar to those in the model (**M1**). However, as the wedge is longer, fewer sediments are accreted at the back for the same amount of shortening.

3.4 Effect of seamount subduction

The seamounts in our models are defined as material with a larger frictional strength, $\phi = 35°$, and larger activation energy than the rest of the material. They are initially located so that, they start to interact with the toe of an M1-type accretionary prism after 7 Myr of simulation time. They all are the same width, and we consider three heights. The large seamount (**M4**) disrupts and emerges above the shallow décollement. The medium height seamount (**M5**) disrupts the shallow décollement but does not emerge, and the smallest one (**M6**) does not disrupt the shallow décollement.

At 7 Myr, seamounts reach the toe of the taper at $x =\sim 340km$. The small seamount, which does not affect the shallow décollement, does not produce deformation of the toe nor modifies the dynamics of the accretionary prism. The two other types of seamounts produce a large shallow dipping thrust fault and some gravitational sliding at the front of the wedge. In these models, during the next 2 Myr, the deformation is accommodated by sliding on a décollement of soft sediments at the front (orange markers in Figure 7) which is mainly by gravitational collapse. At 9 Myr, a new thrust localizes at the front of the wedge above the shallow décollement. After a period of basal erosion, accretion resumes at the front of the prism above the shallow décollement to form a new imbricated zone.

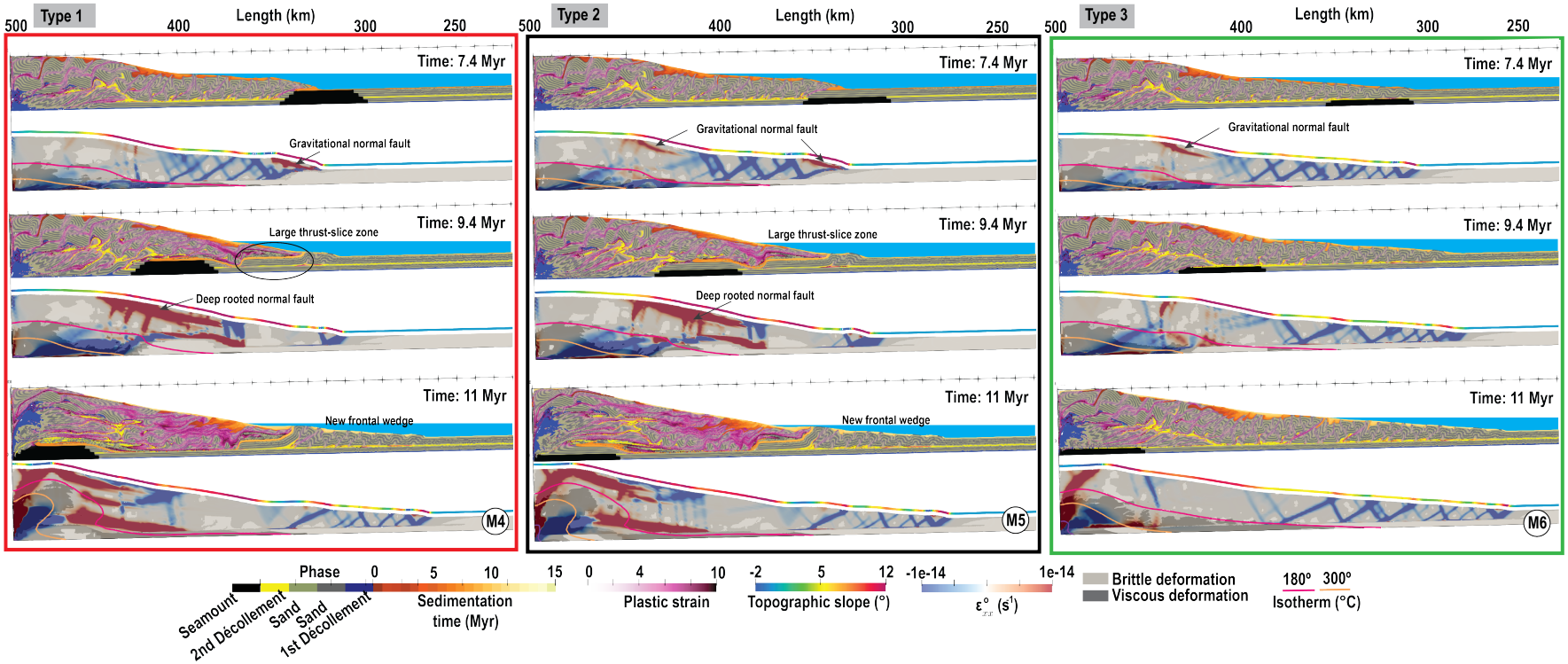

Figure 7: Models with three different initial seamount geometries, large **M4**, medium without décollement on top **M5**, and small size under décollement layer **M6**, 1 : 1 scale.

At the same time, 9 Myr, a set of conjugate normal faults form at the rear of the seamount in between the soft sediment décollement and the shallow décollement. After little deformation, the deformation localizes on the seaward dipping normal fault at the shallow dip. Above this normal fault, a basin forms and accumulates the gravitationally collapsing pieces of the former accretionary prism and new sediments produced by the surface process model. This basin delimits the continent-ward limit of a large slice of undeformed incoming material which serves as a backstop for the new imbricated zone. Since the large piece of undeformed sediment results from the passage of a seamount that has basally eroded the accretionary prism, we consider that the presence of such object on a seismic line marks the suture or the scar of a seamount that has eroded basally the former steady state accretionary prism. In other words, this slice may mark the geological record of a transition from erosion to accretion (provided it is preserved).

The last effect of seamount subduction on our simulations occurs for the three types of seamounts. Indeed, small seamount like larger ones, once subducted, have larger activation energy. Therefore, when they reach the depth at which the temperature along the base of the domain is high enough to induce a deep ductile décollement, underplating ceases for a moment because the seamount is not as sensitive to the temperature as the rest of the accreted material. This is particularly clear in the supplementary movie **M6**, where underplating ceases at 9 Myr and resumes in the last frame at about 12.40 Myr.

4 Discussion of models

4.1 Underplating: a possible marker for the brittle-ductile transition?

Figure 8 represents a synthesis of our model results for a very simplified geological setting using yield strength envelopes. In our simulations, we have used two décollements in order to first build an over critical wedge which could represent the pre-existing outer Makran before the activation of the shallower décollement. Here and in our summary Figure 8, we only consider the final stage of the simulations with a décollement layer at an intermediate depth within the pile of incoming sediments and dismiss the seamount subduction.

At the front of the wedge, the topography and topographic gradient obtained in these simulations are similar to the results obtained for a brittle-ductile wedge with a single basal décollement (Pajang et al., 2021). The toe of the wedge displays a slope which characterizes the frictional strength of the intermediate depth décollement. It is followed by a flat topographic segment that outlines the dehydration reaction zone. Most importantly, the over-critical slope, characterized by the presence of back thrusts and shallow normal faults accommodating gravitational instability is just above the onset of the brittle-ductile transition. The main difference between the models with a unique basal décollement and these models with an intermediate décollement is the accommodation of the deformation at depth.

While models with a unique basal décollement display pure shear shortening above a ductile décollement, models with an intermediate décollement produce underplating. This significant change in model behavior is caused by the onset of the brittle-ductile transition in the sediments located beneath the intermediate décollement. This temperature controlled rheological transition introduces the second décollement in the system. The occurrence of underplating in the presence of two décollements is not new and has been described in many analogue and numerical models e.g. (Bonnet et al., 2007; Stockmal et al., 2007; Kukowski et al., 2002; Ruh et al., 2012; Ruh, 2017, 2020; Menant et al., 2020). Menant et al. (2019) have also investigated the effect of basal underplating on wedge dynamics and topography. The novelty here is that the second décollement is not introduced in the model explicitly but emerges self-consistently at the brittle-ductile transition.

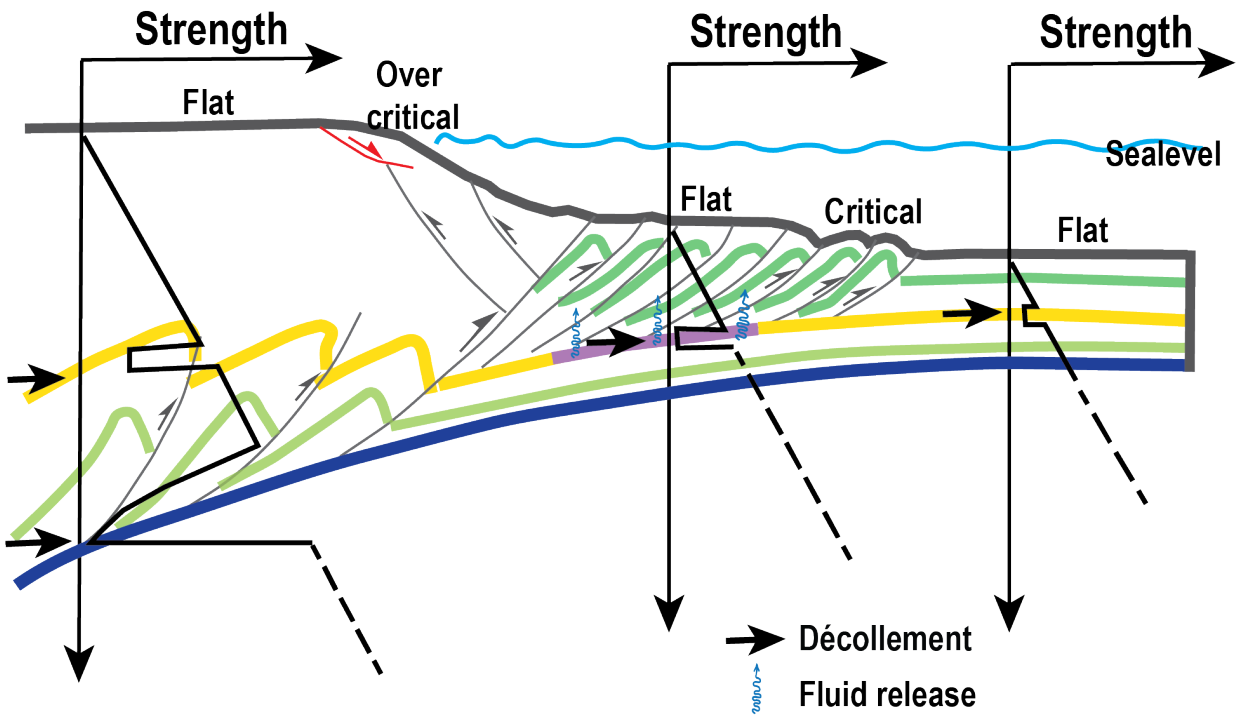

Figure 8: Plot of the strength distribution (yield strength envelope) at the loading axis with depth along the first 30 km of a wedge. The purple segment marks the dehydration reaction window along the shallow décollement.

4.2 The geological signature of seamount subduction

Seamounts or submarine volcanoes migrate together with oceanic plates toward subduction trenches according to plate motion, and, eventually, collide with continental margins where oceanic plates subduct (von Huene, 2008). In terms of deformation, the subduction of seamounts powerfully deforms the overriding plate margin by creating intense fracturing of the upper plate (Wang and Bilek, 2011). Seamounts were studied by analogue, e.g. (Kukowski et al., 1994; Dominguez et al., 1998, 2000) and numerical modeling (Ruh, 2016; Zeumann and Hampel, 2015). They found that:

- Seamount subduction influences the tectonic regime and controls the geodynamic evolution of the whole margin. It is responsible for boosting the tectonic erosion by underthrusting frontal margin material.
- Local variations of pore fluid pressure could result from 1- the underplating of large volumes of undeformed sediments containing fluid beneath the rear part of the seamount and 2- fluid escape through intense fracturing of the upper plate leading to a decrease in the fluid pressure.
- According to numerical modeling, significant overpressure and underpressure areas develop on seamount flanks; compression develops along the wedge toe, and extension close to the rear.
- Strain weakening leads to a slightly more localized fracture system, but displacement generally remains little.
- Large-scale normal faults develop for very weak upper plates.

Our models with two décollements and brittle-ductile transition show that seamount subduction

temporarily affects the length of the flat segment which corresponds to the temperature at which dehydration and possibly fluid overpressure occur.

Dominguez et al. (2000) observed a long tilted zone in the sandbox experiments separating parts of the accretionary wedge developed before and after the seamount subduction and called it a suture zone. Indeed, the slope break of the underplated segment with the frontal segment marks the suture zone. Moore et al. (2001) defined the large-thrust-slice term and mentioned underneath these thrust slices the presence of packages of strong reflectors signing a basement ridge or seamount. Bangs et al. (2006) interpreted these thrusts as primary thrusts because they extend from the décollement at the base of the Nankai Trough subduction zone through the entire wedge to the seafloor. As these large slices are only produced after seamount subduction in our models, we posit that their absence or presence permits to distinguish between underplating due to the shallow décollement or due to seamount subduction. Moreover, we argue that they are the geological signature of a past event of basal erosion in an accretionary prism.

5 Application to Makran

5.1 Underplating and the Pliocene unconformity

The sedimentological data indicates that the emergence of the Makran accretionary prism took place 9-10 Myr ago approximately when the large olistotrome was deposited. The second sign of the emergence is the Late Pliocene age unconformity, which marks the emergence of the coastal area together with the inception of the coastal plateau and the migration of the deformation into the present-day imbricated zone. From numerical modelling, Ruh et al. (2018) proposed that the olistostrome acted as a low-density, low-viscosity layer enabling the growth of gravitationally assisted mini-basins. They suggested that the olistostrome emplacement enhanced underplating and exhumation of the wedge rear and mini-basin subsidence at the front. The shortening would have finally led to horizontal squeezing of the mini-basin province, corresponding to the coastal Makran, and establishing a new imbricated zone ahead. In their models, the olistotrome is added instantaneously in an ad-hoc manner with very low density and viscosity wedge. It momentarily switches off the frontal accretion thanks to intense sedimentation in the mini-basin and the redistribution of the salt-like olistotrome material that keep the topographic slope sub-critical. In our simulations, the uplift at the rear takes place constantly as soon as the brittle-ductile transition is reached and underplating starts. However, the passage of a seamount produces basal erosion and complete collapse of the former accretionary prism. The giant landslide accommodated by deeply rooted normal faults in our simulation could well correspond to the formation of an olistotrome in nature. This collapse redistributes mass enough to shut down frontal accretion and accelerate uplift at the rear for a few million years. However, as the collapsed material in our models does not yield a viscosity as low as 10^{18} Pa.s as in Ruh et al. (2018) study, the simulation does not produce mini-basins. Ruh et al. (2018) model and our models do not contradict each other and are complementary to understand the dynamic of Makran accretionary prism.

Considering two décollements, we found that underplating is associated with viscous deformation. Hence, along Makran, the brittle-ductile transition should coincide with the most frontal underplating slices. None of our models perfectly fit the history of Iranian Makran because they are meant to understand processes. However, they produce large thrusts at the back of the prism corresponding to the initial stage of shortening on the deep décollement (Figure 2). As the shallow décollement gets involved, part of the accretionary prism slides gravitationally and underplating starts beneath the shallow décollement due to the onset of brittle-ductile transition. As the accretionary prism grows, temperature increases with burial and leads to the onset of ductile deformation and the typical splay fault described in Pajang et al. (2022).

With constant frictional properties, surface processes affect the exhumation at the wedge rear. Ac-

cording to Konstantinovskaya and Malavieille (2005), erosion is a necessary condition for exhumation in accretionary prisms. They concluded that the maximum uplift and exhumation occur where antiformal stack duplexes form close to the backstop of their physical experiments. This is comparable with the structure and evolution of the Nepalese Himalaya in the Miocene-Quaternary. We obtained the same results in one of our simulations (**M2**) with high erosion and sedimentation rates. As our models evolve with temperature evolution, underplating does not occur at an early stage, whereas in their experiments underplating starts from the beginning thanks to the addition of glass beads décollement.

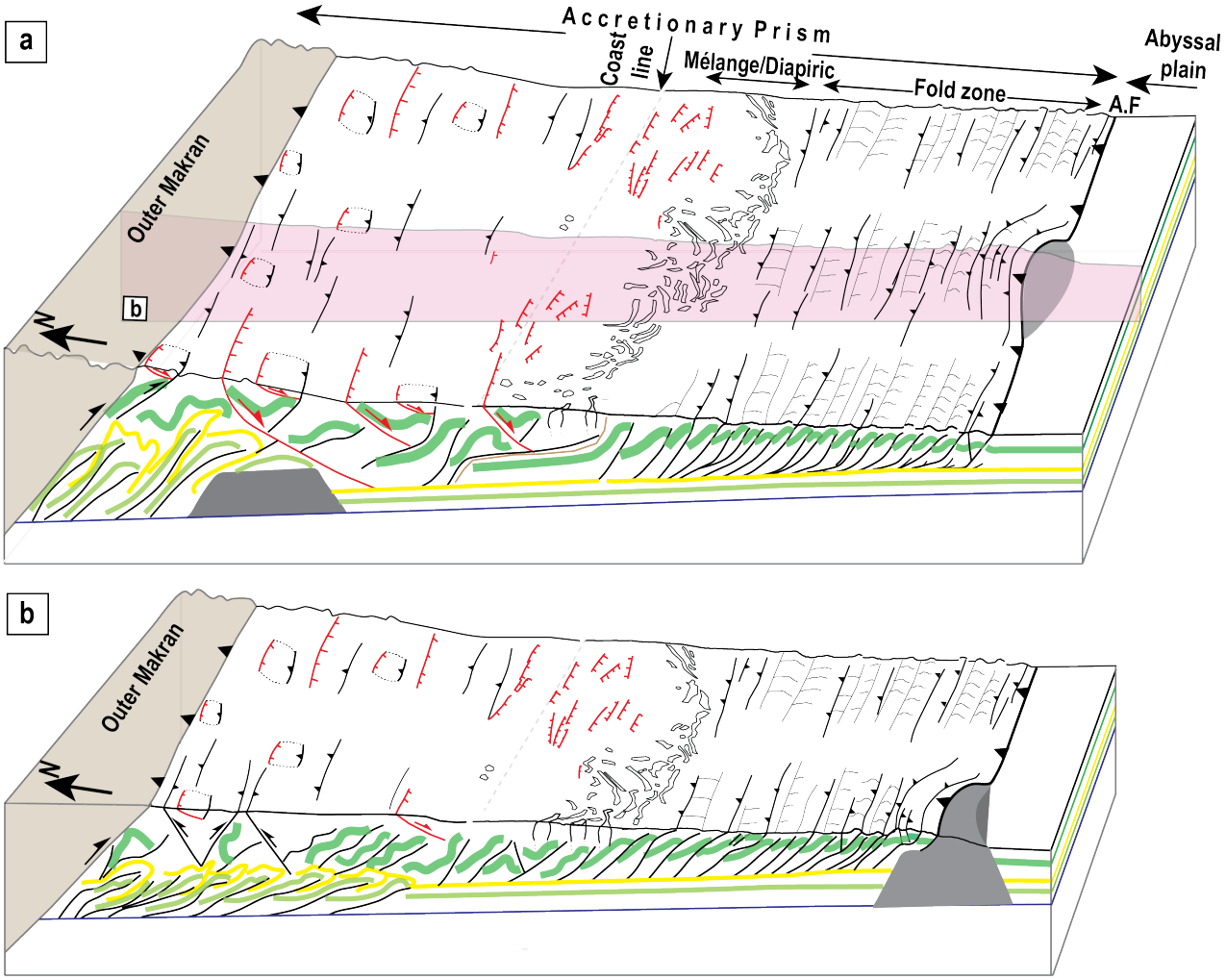

Figure 9: **a.** 3D block diagram across the western Makran along eastern and **b.** central cross-sections. The central section (b) is marked with the purple section on part **a**. See figure 1 for their location.

5.2 Normal faults

According to the critical taper theory, an extremely low basal friction, a very large topographic slope or a decrease of the décollement slope (that could either be related to underplating or seamount subduction) may permit to reach the extensional critical state and hence the formation of normal faults during accretion. However, neither the along-dip drop in friction associated with brittle-ductile transition (a ductile décollement is often considered as equivalent to a very low friction angle) nor the one associated to dehydration reactions hypothesized to favor normal faulting by (Cubas et al., 2013;

Pajang et al., 2021), have been found to be sufficient to get normal faults emerging self- consistently from our long-term simulations. Nonetheless, dewatering during the smectite-illite transition is needed to produce the three slope segments observed in accretionary prisms such as Makran.

Underplating related to the formation of a second décollement at depth changes the basal slope and causes a sharp transition in the topographic slope, which places the wedge at an effective extensional state and leads to the formation of shallow gravitational normal faults but does not permit to form deeply rooted normal faults such as those observed on the seismic profile (Figure 2).

The boosting of the surface slope is caused by the roughness of the plate interface or seamounts form not only gravitational normal faults but also large normal faults rooting down to the décollement. The presence of long-thrust-slices at the back of the imbricated zone are remnant structures indicating the passage of a seamount which is also accompanied by large normal faults whose location migrates through time. These features are in good agreement with our interpretation of the Eastern profile (Figure 2). Hence, the presence of the coastal normal faults is probably related to the subduction of past seamounts.

The salt-like mechanical behaviour of the décollement and mass-transport deposits (MTDs) which are common gravity-induced units in deep-water environments triggered by slope failure, e.g. (Ogata et al., 2014), could also cause the formation of mini-basins and normal faults, but are not accounted for in our simulations.

5.3 A possible model based scenario

We posit that the intermediate depth décollement which serves today as the main décollement level of the imbricated zone entered the Makran accretionary prism some 9 Ma ago (2 Myr model time). It caused the collapse of the former accretionary prism and the establishment of a small imbricated zone at the front. After 5 Myr model time, that is around 6 Ma in nature, the accretionary prism became mature enough for underplating to start in between the brittle-ductile décollement and the shallow décollement, causing both uplift and sporadic activity of normal faults is still observed today. However, given that a seamount is clearly imaged entering the toe of the central profile today, and given that the eastern profile seems to image a large slice at the back of the imbricated zone, we propose to interpret the large velocity anomaly of the tomographic model (Haberland et al., 2020) as a subducted seamount rather than underplating as suggested by the authors. This seamount would have locally eroded the base of the accretionary prism between 5 and 3 Myr ago. Our interpretation is also strengthened by the fact that only the seamount scenario allowed us to generate listric normal fault rooting down to the décollement, as interpreted by Pajang et al. (2021). All our interpretations are represented in a 3D diagram along the Iranian part of the Makran prism (Figure 9).

5.4 Limitations and perspectives

Contrarily to the static critical taper theory based approached of Cubas et al. (2016) and Pajang et al. (2021) the large along-dip drop in friction introduced by our parametrization was not sufficient to produce normal faults that are observed along the Makran margin. Moreover, due to the presence of shale and mud, the quality of the seismic data near the coast of the selected profiles is quite poor, and the relationship between the normal faults and the underplating is difficult to establish. In our current understanding, despite all the parameters and models tested above, only the seamount scenario allowed us to generate large normal faults. Yet, we would like to emphasize that we considered only the effect of dehydration reaction (friction drop) but fluid release is absent.

In our models, we need to have extremely low friction on the décollement to explain the three slope segments observed in the Makran accretionary prism. We introduce this drop of friction with a parametrization of dehydration reaction described in Pajang et al. (2022). Fluid overpressure due to dehydration of shale materials which potentially corresponds to smectite-illite transition has already

been discussed, e.g. (Pytte and Reynolds, 1988; Hyndman et al., 1995; Oleskevich et al., 1999). During dehydration reaction along the décollement, fluids are released in the clay-rich décollement of low permeability permitting to build of strong local fluid overpressure (Bekins et al., 1994; Lanson et al., 2009). This overpressure zone is associated with an extremely low effective friction angle causes a distinct flat domain that is also suitable for creating mud volcanoes.

Our parameterization of dehydration differs from that of Ellis et al. (2015) who considered that the main source of fluid was the compaction of low permeability underplated sediments. In their formulation the décollement was a high permeability zone, which drains the deep fluids out at the front of the wedge thanks to frequent fractures. The two parametrizations differ a lot in terms on friction on the décollement and that of Ellis et al. (2015), if plugged into pTatin2d would not produce the low slope segment. To reconcile the two approaches, we need to think in terms of time integral over a seismic cycle. Ellis et al. (2015) indeed attempt to model fluid flow over several seismic cycles in a fixed geometry deduced from seismic data. They are right to consider that over several seismic cycles the décollement is a high permeability zone in their water budget. Yet, as stated earlier, large fluid overpressure in the décollement is needed in order to produce the correct topographic slope of Makran both in our long-term tectonic model and in the critical taper theory based approach of Pajang et al. (2021). The reconciliation between the two parametrizations is that the fluid pressure in our model needs to reflect the friction / effective strength of the décollement during the slip event, while the permeability in Ellis et al. (2015) reflects a time integral over the seismic cycle. Modelling the entire seismic cycle with fluid flow, as in Dal Zilio and Gerya (2022), shows that time variations of friction along the décollement are expected during the seismic cycle when accurate coupling with fluid is implemented. The way forward should be to couple this type of approach with a long-term tectonic model that can actually build the long-term tectonic slope. This will be helpful to test the original hypothesis of Cubas et al. (2016), which posit that large deeply rooted normal faults might form by dynamic periodic decrease of the effective megathrust friction during an earthquake. Moreover, true coupling with fluid would also certainly modify heat flow locally, heating up the faults with a deep fluid release towards the surface and cooling down the basal décollement making it more prone to brittle deformation.

6 Conclusions

In this study, geometric analysis confirms that ∼50 percent of the incoming ∼7.5 km thick sedimentary sequence must be underthrusted along a secondary décollement and stacked further to the rear of the wedge as proposed by (Platt and Leggett, 1986) and confirmed by Ruh (2020). Two cross-sections are presented which are aligned with two offshore profiles that were previously balanced (Pajang et al., 2021) and with recently published seismic tomography models (Haberland et al., 2020). In order to ameliorate our interpretation in depth, we have run thermomechanically coupled simulations of the formation of accretionary prism, focusing mainly on the role of the smectite-illite transition, underplating and seamounts subduction. The models have been calibrated by picking the BSR on the available seismic data and interpreting it in terms of heat flow.

The simulations show that dewatering and smectite-illite transition together can produce the three slope segments previously documented in Makran. Seamounts subduction does not affect the slope for a very long time but permits the formation of large tectonic slices and deeply rooted normal faults that cannot be formed with a second décollement alone. The lateral extent of these normal faults would typically be limited by the width of the seamount entering the subduction zone.

Our new cross-sections are compatible with a late Pliocene coast-line uplift which would correspond to the onset of ductile décollement and splay fault system and can explain the large slope observed at the coast. The passage of eventual seamount changes the shape of the thrust slices at depth.

A Equations

pTatin2D (May et al., 2014, 2015) is a code based on the finite element method that employs an arbitrary LagrangianEulerian (ALE) discretization together with the material point method to solve the conservation of momentum (Eq. 1), mass (Eq. 2) and, energy (Eq. 3) for an incompressible fluid. It allows solving thermo-mechanical problems. The codes solve for velocity v and pressure P assuming conservation of momentum:

$$\nabla \cdot (2\eta \dot{\boldsymbol{\varepsilon}}) - \nabla P = \rho \mathbf{g}, \tag{1}$$

in an incompressible fluid:

$$\nabla \cdot \mathbf{v} = 0, \tag{2}$$

of nonlinear effective viscosity η and constant density ρ, $\dot{\boldsymbol{\varepsilon}}$ being the strain rate tensor and g the gravity acceleration. The evolution of temperature T is obtained by solving for transient conservation of heat of the form:

$$\frac{\partial T}{\partial t} = \nabla \cdot (\kappa \nabla T) - v \nabla T + \frac{H}{\rho Cp}. \tag{3}$$

where t is time, κ the thermal diffusivity, Cp the heat capacity, and the heat production H defined as:

$$H = \tau_{ij} \dot{\varepsilon}_{ij} = 2\eta(\dot{\varepsilon}_{xx}^2 + 2\dot{\varepsilon}_{xy}^2 + \dot{\varepsilon}_{yy}^2) \tag{4}$$

corresponds to shear heating in this contribution. The Stokes problem is solved using high stable order elements (Q_2P_1), while the heat equation is discretized on Q_1 elements. At every time step, the surface of the models is smoothed according to Culling erosion law defined as:

$$\frac{\partial h}{\partial t} = -\nabla \cdot (k \nabla h) \tag{5}$$

where h is the altitude and k is the constant diffusion coefficient. We do not account for sea level in the erosion sedimentation implementation. Details on implementation of the surface process model in pTatin2d are found in Jourdon et al. (2018). We use temperature and pressure-dependent nonlinear rheologies. Effective viscosity is evaluated on material points using first the Arrhenius flow law for dislocation creep:

$$\eta_{\text{vis}} = A^{-\frac{1}{n}} \left(\dot{\varepsilon}^{\text{II}}\right)^{\frac{1}{n-1}} \exp\left(\frac{Q + PV}{nRT}\right) \tag{6}$$

If the stress predicted with viscous creep and current strain rate exceeds Drucker-Prager plastic yield criterion, defined as:

$$\sigma_Y = \sin\phi P + C\cos\phi \tag{7}$$

with ϕ the friction angle and C the cohesion, the effective viscosity of the marker is corrected in order to fit the yield envelop:

$$\eta_p = \frac{\sigma_Y}{2\dot{\varepsilon}^{II}}. \tag{8}$$

for the current value of the second invariant of the strain rate tensor $\dot{\varepsilon}^{II}$. The friction angle ϕ and cohesion C decrease linearly with an accumulation of strain in the plastic regime ε_p from an initial friction ϕ_0 to a final friction ϕ_∞ (resp. C_0 and C_∞ for cohesion):

$$\phi = \phi_0 - \frac{\varepsilon_p - \varepsilon_{\min}}{\varepsilon_{\max} - \varepsilon_{\min}} \left(\phi_0 - \phi_\infty\right), \tag{9}$$

In every element, we use logarithmic averaging for viscosity and arithmetic averaging for density, projection from marker to integration point is a P0 (constant) projection.

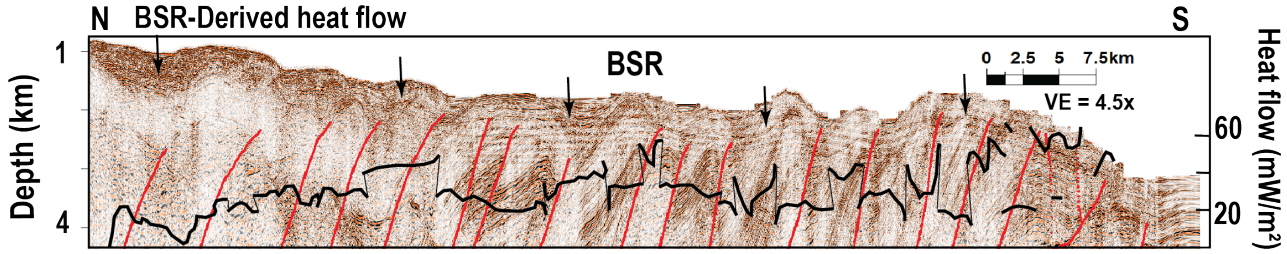

Figure 10: Zoom-in of Central offshore migrated profile. The BSR is indicated by black arrows, the BSR-derived heat flow is shown in black.

B Supplementary figure

Video supplement: All the simulation videos are available.

Code availability: The version of pTatin2d and the input files used in this study are archived following the FAIR principle at `https://doi.org/10.5281/zenodo.4911354` (May and Le Pourhiet, 2021).

References

Babadi, M. F., Mehrabi, B., Tassi, F., Cabassi, J., Vaselli, O., Shakeri, A., Pecchioni, E., Venturi, S., Zelenski, M., Chaplygin, I., 2019. Origin of fluids discharged from mud volcanoes in se iran. Marine and Petroleum Geology 106, 190–205.

Bangs, N. L., Gulick, S. P., Shipley, T. H., 2006. Seamount subduction erosion in the nankai trough and its potential impact on the seismogenic zone. Geology 34 (8), 701–704.

Bekins, B., McCaffrey, A. M., Dreiss, S. J., 1994. Influence of kinetics on the smectite to illite transition in the barbados accretionary prism. Journal of Geophysical Research: Solid Earth 99 (B9), 18147–18158.

Bonnet, C., Malavieille, J., Mosar, J., 2007. Interactions between tectonics, erosion, and sedimentation during the recent evolution of the alpine orogen: Analogue modeling insights. Tectonics 26 (6).

Buiter, S. J., Schreurs, G., Albertz, M., Gerya, T. V., Kaus, B., Landry, W., Le Pourhiet, L., Mishin, Y., Egholm, D. L., Cooke, M., et al., 2016. Benchmarking numerical models of brittle thrust wedges. Journal of Structural Geology 92, 140–177.

Burg, J.-P., 2018. Geology of the onshore makran accretionary wedge: Synthesis and tectonic interpretation. Earth-Science Reviews 185, 1210–1231.

Burg, J.-P., Bernoulli, D., Smit, J., Dolati, A., Bahroudi, A., 2008. A giant catastrophic mud-and-debris flow in the miocene makran. Terra Nova 20 (3), 188–193.

Burg, J.-P., Dolati, A., Bernoulli, D., Smit, J., 2012. Structural style of the makran tertiary accretionary complex in se-iran. In: Lithosphere dynamics and sedimentary basins: The Arabian Plate and analogues. Springer, pp. 239–259.

Cubas, N., Avouac, J.-P., Leroy, Y. M., Pons, A., 2013. Low friction along the high slip patch of the 2011 mw 9.0 tohoku-oki earthquake required from the wedge structure and extensional splay faults. Geophysical Research Letters 40 (16), 4231–4237.

Cubas, N., Souloumiac, P., Singh, S. C., 2016. Relationship link between landward vergence in accretionary prisms and tsunami generation. Geology 44 (10), 787–790.

Dal Zilio, L., Gerya, T., 2022. Subduction earthquake cycles controlled by episodic fluid pressure cycling. Lithos, 106800.

DeMets, C., Gordon, R. G., Argus, D. F., 2010. Geologically current plate motions. Geophysical Journal International 181 (1), 1–80.

Dholabhai, P., Englezos, P., Kalogerakis, N., Bishnoi, P., 1991. Equilibrium conditions for methane hydrate formation in aqueous mixed electrolyte solutions. The Canadian journal of chemical engineering 69 (3), 800–805.

Dickens, G. R., Quinby-Hunt, M. S., 1994. Methane hydrate stability in seawater. Geophysical Research Letters 21 (19), 2115–2118.

Dolati, A., 2010. Stratigraphy, structural geology and low-temperature thermochronology across the makran accretionary wedge in iran. Ph.D. thesis, ETH Zurich.

Dominguez, S., Lallemand, S., Malavieille, J., von Huene, R., 1998. Upper plate deformation associated with seamount subduction. Tectonophysics 293 (3-4), 207–224.

Dominguez, S., Malavieille, J., Lallemand, S. E., 2000. Deformation of accretionary wedges in response to seamount subduction: Insights from sandbox experiments. Tectonics 19 (1), 182–196.

Ellis, S., Fagereng, Å., Barker, D., Henrys, S., Saffer, D., Wallace, L., Williams, C., Harris, R., 2015. Fluid budgets along the northern hikurangi subduction margin, new zealand: The effect of a subducting seamount on fluid pressure. Geophysical Journal International 202 (1), 277–297.

Ellouz-Zimmermann, N., Deville, E., Müller, C., Lallemant, S., Subhani, A., Tabreez, A., 2007a. Impact of sedimentation on convergent margin tectonics: Example of the makran accretionary prism (pakistan). In: Thrust Belts and Foreland Basins. Springer, pp. 327–350.

Ellouz-Zimmermann, N., Lallemant, S., Castilla, R., Mouchot, N., Leturmy, P., Battani, A., Buret, C., Cherel, L., Desaubliaux, G., Deville, E., et al., 2007b. Offshore frontal part of the makran accretionary prism: The chamak survey (pakistan). In: Thrust belts and foreland basins. Springer, pp. 351–366.

Englezos, P., Bishnoi, P., 1988. Gibbs free energy analysis for the supersaturation limits of methane in liquid water and the hydrate-gas-liquid water phase behavior. Fluid Phase Equilibria 42, 129–140.

Falcon, N., 1975. From musandam to iranian makran. Geographical Journal 141 (MAR), 55–58.

Farhoudi, G., Karig, D., 1977. Makran of iran and pakistan as an active arc system. Geology 5 (11), 664–668.

Ganguly, N., Spence, G., Chapman, N., Hyndman, R., 2000. Heat flow variations from bottom simulating reflectors on the cascadia margin. Marine geology 164 (1-2), 53–68.

Grando, G., McClay, K., 2007. Morphotectonics domains and structural styles in the makran accretionary prism, offshore iran. Sedimentary Geology 196 (1-4), 157–179.

Grevemeyer, I., Villinger, H., 2001. Gas hydrate stability and the assessment of heat flow through continental margins. Geophysical Journal International 145 (3), 647–660.

Haberland, C., Mokhtari, M., Babaei, H. A., Ryberg, T., Masoodi, M., Partabian, A., Lauterjung, J., 2020. Anatomy of a crustal-scale accretionary complex: Insights from deep seismic sounding of the onshore western makran subduction zone, iran. Geology 49 (1), 3–7.

Haghipour, N., Burg, J.-P., Ivy-Ochs, S., Hajdas, I., Kubik, P., Christl, M., 2015. Correlation of fluvial terraces and temporal steady-state incision on the onshore makran accretionary wedge in southeastern iran: Insight from channel profiles and 10be exposure dating of strath terraces. Bulletin 127 (3-4), 560–583.

Haghipour, N., Burg, J.-P., Kober, F., Zeilinger, G., Ivy-Ochs, S., Kubik, P. W., Faridi, M., 2012. Rate of crustal shortening and non-coulomb behaviour of an active accretionary wedge: The folded fluvial terraces in makran (se, iran). Earth and Planetary Science Letters 355, 187–198.

Hutchison, I., Louden, K., White, R., Von Herzen, R., 1981. Heat flow and age of the gulf of oman. Earth and Planetary Science Letters 56, 252–262.

Hyndman, R., Wang, K., Yamano, M., 1995. Thermal constraints on the seismogenic portion of the southwestern japan subduction thrust. Journal of Geophysical Research: Solid Earth 100 (B8), 15373–15392.

Hyndman, R. D., Wang, K., 1993. Thermal constraints on the zone of major thrust earthquake failure: The cascadia subduction zone. Journal of Geophysical Research: Solid Earth 98 (B2), 2039–2060.

Jourdon, A., Le Pourhiet, L., Petit, C., Rolland, Y., 2018. Impact of range-parallel sediment transport on 2d thermo-mechanical models of mountain belts: Application to the kyrgyz tien shan. Terra Nova 30 (4), 279–288.

Kaul, N., Rosenberger, A., Villinger, H., 2000. Comparison of measured and bsr-derived heat flow values, makran accretionary prism, pakistan. Marine Geology 164 (1-2), 37–51.

Khan, M., Raza, H. A., Alam, S., 1991. Petroleum geology of the makran region: implications for hydrocarbon occurrence in cool basins. Journal of Petroleum Geology 14 (1), 5–18.

Kinoshita, M., Moore, G. F., Kido, Y. N., 2011. Heat flow estimated from bsr and iodp borehole data: Implication of recent uplift and erosion of the imbricate thrust zone in the nankai trough off kumano. Geochemistry, Geophysics, Geosystems 12 (9).

Konstantinovskaya, E., Malavieille, J., 2005. Accretionary orogens: erosion and exhumation. Geotectonics 39 (1), 69–86.

Konstantinovskaya, E., Malavieille, J., 2011. Thrust wedges with décollement levels and syntectonic erosion: A view from analog models. Tectonophysics 502 (3-4), 336–350.

Kopp, C., Fruehn, J., Flueh, E., Reichert, C., Kukowski, N., Bialas, J., Klaeschen, D., 2000. Structure of the makran subduction zone from wide-angle and reflection seismic data. Tectonophysics 329 (1-4), 171–191.

Kukowski, N., Lallemand, S. E., Malavieille, J., Gutscher, M.-A., Reston, T. J., 2002. Mechanical decoupling and basal duplex formation observed in sandbox experiments with application to the western mediterranean ridge accretionary complex. Marine Geology 186 (1-2), 29–42.

Kukowski, N., Schillhorn, T., Huhn, K., von Rad, U., Husen, S., Flueh, E. R., 2001. Morphotectonics and mechanics of the central makran accretionary wedge off pakistan. Marine Geology 173 (1-4), 1–19.

Kukowski, N., Von Huene, R., Malavieille, J., Lallemand, S., 1994. Sediment accretion against a buttress beneath the peruvian continental margin at 12 s as simulated with sandbox modeling. Geologische Rundschau 83 (4), 822–831.

Lanson, B., Sakharov, B. A., Claret, F., Drits, V. A., 2009. Diagenetic smectite-to-illite transition in clay-rich sediments: A reappraisal of x-ray diffraction results using the multi-specimen method. American Journal of Science 309 (6), 476–516.

MacLeod, M., 1982. Gas hydrates in ocean bottom sediments. AAPG Bulletin 66 (12), 2649–2662.

Maekawa, T., 2001. Equilibrium conditions for gas hydrates of methane and ethane mixtures in pure water and sodium chloride solution. Geochemical Journal 35 (1), 59–66.

Marcaillou, B., Spence, G., Collot, J.-Y., Wang, K., 2006. Thermal regime from bottom simulating reflectors along the north ecuador–south colombia margin: Relation to margin segmentation and great subduction earthquakes. Journal of Geophysical Research: Solid Earth 111 (B12).

Martin, R. C., Dahlen, E. R., 2005. Cognitive emotion regulation in the prediction of depression, anxiety, stress, and anger. Personality and individual differences 39 (7), 1249–1260.

May, D. A., Brown, J., Le Pourhiet, L., 2014. ptatin3d: High-performance methods for long-term lithospheric dynamics. In: SC'14: Proceedings of the International Conference for High Performance Computing, Networking, Storage and Analysis. IEEE, pp. 274–284.

May, D. A., Brown, J., Le Pourhiet, L., 2015. A scalable, matrix-free multigrid preconditioner for finite element discretizations of heterogeneous stokes flow. Computer methods in applied mechanics and engineering 290, 496–523.

Menant, A., Angiboust, S., Gerya, T., 2019. Stress-driven fluid flow controls long-term megathrust strength and deep accretionary dynamics. Scientific reports 9 (1), 1–11.

Menant, A., Angiboust, S., Gerya, T., Lacassin, R., Simoes, M., Grandin, R., 2020. Transient stripping of subducting slabs controls periodic forearc uplift. Nature Communications 11 (1), 1–10.

Miles, P., 1995. Potential distribution of methane hydrate beneath the european continental margins. Geophysical Research Letters 22 (23), 3179–3182.

Minshull, T., White, R., 1989. Sediment compaction and fluid migration in the makran accretionary prism. Journal of Geophysical Research: Solid Earth 94 (B6), 7387–7402.

Mohammadi, A., Burg, J.-P., Winkler, W., Ruh, J., von Quadt, A., 2016. Detrital zircon and provenance analysis of late cretaceous–miocene onshore iranian makran strata: Implications for the tectonic setting. GSA Bulletin 128 (9-10), 1481–1499.

Moore, G., Taira, A., Bangs, N., Kuramoto, S., Shipley, T., Alex, C., Gulick, S., Hills, D., Ike, T., Ito, S., et al., 2001. 2. data report: Structural setting of the leg 190 muroto transect1. Report, 1–14.

Normand, R., Simpson, G., Bahroudi, A., 2019. Extension at the coast of the makran subduction zone (iran). Terra Nova 31 (6), 503–510.

Ogata, K., Pogačnik, Ž., Pini, G. A., Tunis, G., Festa, A., Camerlenghi, A., Rebesco, M., 2014. The carbonate mass transport deposits of the paleogene friuli basin (italy/slovenia): internal anatomy and inferred genetic processes. Marine Geology 356, 88–110.

Ohde, A., Otsuka, H., Kioka, A., Ashi, J., 2018. Distribution and depth of bottom-simulating reflectors in the nankai subduction margin. Earth, Planets and Space 70 (1), 1–20.

Oleskevich, D., Hyndman, R., Wang, K., 1999. The updip and downdip limits to great subduction earthquakes: Thermal and structural models of cascadia, south alaska, sw japan, and chile. Journal of Geophysical Research: Solid Earth 104 (B7), 14965–14991.

Page, W. D., Alt, J. N., Cluff, L. S., Plafker, G., 1979. Evidence for the recurrence of large-magnitude earthquakes along the makran coast of iran and pakistan. Tectonophysics 52 (1-4), 533–547.

Pajang, S., Cubas, N., Letouzey, J., Le Pourhiet, L., Seyedali, S., Fournier, M., Agard, P., Khatib, M. M., Heyhat, M., Mokhtari, M., 2021. Seismic hazard of the western makran subduction zone: insight from mechanical modelling and inferred frictional properties. Earth and Planetary Science Letters 562, 116789.

Pajang, S., Le Pourhiet, L., Cubas, N., 2022. The topographic signature of temperature-controlled rheological transitions in an accretionary prism. Solid Earth 13 (3), 535–551.

Phrampus, B. J., Harris, R. N., Tréhu, A. M., 2017. Heat flow bounds over the c ascadia margin derived from bottom simulating reflectors and implications for thermal models of subduction. Geochemistry, Geophysics, Geosystems 18 (9), 3309–3326.

Platt, J. P., Leggett, J. K., 1986. Stratal extension in thrust footwalls, makran accretionary prism: implications for thrust tectonics. AAPG Bulletin 70 (2), 191–203.

Platt, J. P., Leggett, J. K., Alam, S., 1988. Slip vectors and fault mechanics in the makran accretionary wedge, southwest pakistan. Journal of Geophysical Research: Solid Earth 93 (B7), 7955–7973.

Pytte, A., Reynolds, R., 1988. The thermal transformation of smectite to illite. pp. 133ā140 in: Thermal history of sedimentary basins (nd naeser and th mcculloh, editors).

Quintero, W., Campos-Enríquez, O., Hernández, O., 2019. Curie point depth, thermal gradient, and heat flow in the colombian caribbean (northwestern south america). Geothermal Energy 7 (1), 1–20.

Ranalli, G., Murphy, D. C., 1987. Rheological stratification of the lithosphere. Tectonophysics 132 (4), 281–295.

Ruh, J. B., 2016. Submarine landslides caused by seamounts entering accretionary wedge systems. Terra Nova 28 (3), 163–170.

Ruh, J. B., 2017. Effect of fluid pressure distribution on the structural evolution of accretionary wedges. Terra Nova 29 (3), 202–210.

Ruh, J. B., 2020. Numerical modeling of tectonic underplating in accretionary wedge systems. Geosphere 16 (6), 1385–1407.

Ruh, J. B., Kaus, B. J., Burg, J.-P., 2012. Numerical investigation of deformation mechanics in fold-and-thrust belts: Influence of rheology of single and multiple décollements. Tectonics 31 (3).

Ruh, J. B., Vergés, J., Burg, J.-P., 2018. Shale-related minibasins atop a massive olistostrome in an active accretionary wedge setting: Two-dimensional numerical modeling applied to the iranian makran. Geology 46 (9), 791–794.

Sain, K., Minshull, T., Singh, S., Hobbs, R., 2000. Evidence for a thick free gas layer beneath the bottom simulating reflector in the makran accretionary prism. Marine Geology 164 (1-2), 3–12.

Schlüter, H., Prexl, A., Gaedicke, C., Roeser, H., Reichert, C., Meyer, H., Von Daniels, C., 2002. The makran accretionary wedge: sediment thicknesses and ages and the origin of mud volcanoes. Marine Geology 185 (3-4), 219–232.

Shea, W. T., Kronenberg, A. K., 1992. Rheology and deformation mechanisms of an isotropic mica schist. Journal of Geophysical Research: Solid Earth 97 (B11), 15201–15237.

Skarpnes, O., Skinnemoen, ., Scotchmer, J., 2003. Nioc-statoil joint exploration study oman sea. Unpublished NIOC-Statoil Report 1, 154.

Stockmal, G. S., Beaumont, C., Nguyen, M., Lee, B., Sears, J., 2007. Mechanics of thin-skinned fold-and-thrust belts: Insights from numerical models. SPECIAL PAPERS-GEOLOGICAL SOCIETY OF AMERICA 433, 63.

Sultan, N., Foucher, J.-P., Cochonat, P., Tonnerre, T., Bourillet, J.-F., Ondreas, H., Cauquil, E., Grauls, D., 2004. Dynamics of gas hydrate: case of the congo continental slope. Marine Geology 206 (1-4), 1–18.

Tishchenko, P., Hensen, C., Wallmann, K., Wong, C. S., 2005. Calculation of the stability and solubility of methane hydrate in seawater. Chemical geology 219 (1-4), 37–52.

Turcotte, D. L., Schubert, G., 2002. Geodynamics. Cambridge university press.

Villar-Muñoz, L., Behrmann, J. H., Diaz-Naveas, J., Klaeschen, D., Karstens, J., 2014. Heat flow in the southern chile forearc controlled by large-scale tectonic processes. Geo-Marine Letters 34 (2), 185–198.

Villar-Muñoz, L., Vargas-Cordero, I., Bento, J. P., Tinivella, U., Fernandoy, F., Giustiniani, M., Behrmann, J. H., Calderón-Díaz, S., 2019. Gas hydrate estimate in an area of deformation and high heat flow at the chile triple junction. Geosciences 9 (1), 28.

Vita-Finzi, C., 1975. Quaternary deposits in the iranian makran. Geographical Journal, 415–420.

von Huene, R., 2008. When seamounts subduct. Science 321 (5893), 1165–1166.

Wang, K., Bilek, S. L., 2011. Do subducting seamounts generate or stop large earthquakes? Geology 39 (9), 819–822.

Zeumann, S., Hampel, A., 2015. Deformation of erosive and accretive forearcs during subduction of migrating and non-migrating aseismic ridges: Results from 3-d finite element models and application to the central american, peruvian, and ryukyu margins. Tectonics 34 (9), 1769–1791.